54th AIAA/ASME/ASCE/AHS/ASC Structures, Structural Dynamics, and Materials Conference AIAA 2013-1908
April 8-11, 2013, Boston, Massachusetts

Fluid–Structure Interaction Analysis of the Fish Bone Active Camber Mechanism

Benjamin K. S. Woods[1]
Swansea University, Swansea, UK, SA2 8PP

Michael I. Friswell [2]
Swansea University, Swansea, UK, SA2 8PP

A strongly coupled, partitioned fluid–structure interaction analysis is introduced which allows for calculation of the deformed equilibrium shape and actuation requirements of the Fish Bone Active Camber mechanism under quasi-static aerodynamic loading. The Fish Bone Active Camber mechanism has recently been introduced as a high authority morphing camber architecture with a broad range of applications; including fixed wing aircraft, helicopters, wind turbines, and tidal stream turbines. This design employs a biologically inspired compliant structure to create continuous changes in airfoil camber and aerodynamic properties. The structure consists of a thin chordwise bending beam spine with stringers branching off to connect it to a pre-tensioned Elastomeric Matrix Composite skin surface. An actuation system mounted in a rigid D-spar induces bending moments on the spine through an antagonistic pair of tendons in a manner similar to natural musculature systems. The low bending stiffness of the primary structure, high stiffness of the tendons, and the large changes in aerodynamic loading while morphing necessitate a fully coupled fluid–structure interaction analysis for determination of the static equilibrium at different operating conditions. An Euler–Bernoulli beam theory based analytical model of the structure is introduced. Aerodynamic pressure distributions on the skin surface are found using XFOIL software, which couples a panel method with a viscous boundary layer solver. Finally, the tendons are modeled as linear stiffness elements whose internal strains are found from Euler–Bernoulli theory and whose axial forces create bending moments on the spine at their discrete mounting points. Convergence of the FSI code is stabilized through incorporation of relaxation parameters to the tendon moments and deflected shape.

I. Introduction

THE development of compliance based approaches for morphing aircraft structures requires careful consideration of the methods used to model the aerodynamic and structural performance. Typically, if the deflections achieved with the morphing structure are large, then the coupling between aerodynamic and structural loads will be strong. For this reason, fluid–structure interaction (FSI) analysis is crucial to successful prediction of performance for these concepts. This work focuses on the development of an FSI code for a newly developed camber morphing concept known as the Fish Bone Active Camber (FishBAC) mechanism. An overview of previous compliance based camber morphing concepts will be provided, along with a review of FSI methods applied to complaint morphing concepts. After this the design philosophy of the FishBAC concept will be briefly presented. The two partitions of the FSI code, the aerodynamic and structural solvers, will then be detailed and the coupling of the two will be discussed, with special attention paid to the relaxation parameters employed to ensure stability and convergence of the algorithm. Finally, results from the FSI code will be shown for a representative design case.

---

[1] Research Officer, College of Engineering, Regular Member.
[2] Professor, College of Engineering.

II. Background

A significant amount of research has been put into the pursuit of compliant morphing camber mechanisms for both fixed and rotating wing applications. The many different concepts explored over the last several decades have been summarized in several review papers.[1,2,3] Much of this work has been focused on the development of active rotor systems for helicopters and tilt rotors. The two most successful active rotor concepts to date have been developed to the point of full scale wind tunnel testing and flight testing. Straub *et al*. have developed a hinged trailing edge flap driven by piezoelectric stacks with mechanical stroke amplification.[4] While this design is more akin to a traditional trailing edge flap (albeit with smart material actuation) than to a continuous camber morph, extensive open and closed loop vibration reduction testing was performed over a broad range of operating conditions in the NASA 40x80ft wind tunnel. Eurocopter has flight tested a similar piezo driven trailing edge flap system on a highly instrumented BK117.[5] EADS, the parent company of Eurocopter, has also developed a continuous active camber morph driven by piezoelectric benders.[6] While these designs have shown significant potential to reduce vibration, they do so with fairly modest camber deflections and incremental changes to the local airfoil properties. Flap deflections obtained are on the order of several degrees. As such, they do not provide large magnitude changes to vehicle performance. While significant changes to rotor thrust are reported by Straub *et al.*, the primary goals are to increase pilot and passenger comfort and to reduce noise.[4] A morphing rotor system with sufficient control authority to provide primary control or to allow for significant reconfiguring of rotor properties remains an active area of research.

Other concepts are being pursued for fixed wing applications that are intended to create larger changes in airfoil properties. Barbarino *et al*. provide a thorough overview of work done to date.[3] Of particular interest to this discussion are concepts which create smooth, continuous camber change. The DARPA Smart Wing program included a compliant trailing edge morphing structure.[7] This structure consisted of a central laminate with honeycomb on top and bottom to support a flexible silicone skin. This concept was actuated by an “eccentuator”, which employs a rotating kinked rod that transforms the rotary motion of a piezoelectric motor into thickness-wise translation of several points along the chord of the morphing section, thereby creating a smooth bending deflection. A gear box was used to increase the torque output of the motors, at the expense of bandwidth. Wind tunnel testing on a UAV model fitted with a morphing trailing edge showed large deflections under aerodynamic loads up to $M = 0.8$. While changes to section properties are not presented, total vehicle control moments are shown, and the concept is able to provide reasonable control authority to the vehicle.

A related concept is under investigation for wind turbine applications by Daynes and Weaver.[8] Here, the laminate structure is moved out of the center of the section to become the upper skin surface, which is connected to the lower silicone skin surface through a Nomex honeycomb core. Actuation is provided by a gear motor acting through a rigid push-pull rod connected to the trailing edge. The undesirable anticlastic curvature effects caused by the large Poisson’s ratio of the core are reduced by making a series of chordwise cuts through the core every 20 mm. Wind tunnel testing of this concept at speeds up to 56 m/s showed good control authority, with changes to the local lift coefficient on the order of $\Delta C_l = \pm 0.5$ for a 20% chord morphing flap.[8]

Concepts which employ compliant structures to achieve camber change will invariably need to consider the effects of aerodynamic loading on the deformed shape of the structure. This stems from the fact that designing a structure to be deflected with reasonable actuation loads generally leads to a level of compliance that will allow for aerodynamic loading to have a significant impact on deformed shape. This therefore requires the use of coupled fluid–structure interaction solvers to properly account for aerodynamic induced deflections to solve for equilibrium deflections. Bae, Kyong, Seigler and Inman showed the importance of aerodynamic induced deformations for a morphing UAV using piezoelectric actuators to induce camber change.[9] Campanile and Anders studied aerodynamic deformations and aeroelastic amplification in the belt rib concept proposed by DLR.[10] Barbarino *et al.* present the effect of aerodynamic loading on an SMA driven active camber concept, but do not use a coupled solver.[11] Bilgen, Saavedra Flores, and Friswell present a strongly coupled, partitioned FSI solver and optimizer for a thin shell morphing airfoil driven by skin mounted MFC actuators.[12] De Gaspari and Ricci present a two level optimization routine for morphing camber design using FSI and genetic algorithms.[13] Daynes and Weaver present a staged FSI analysis of a morphing wind turbine blade wherein the static solution is first found without aerodynamic loading, after which the aerodynamic load was applied and the code run again until convergence.[8] Molinari *et al.*[14] and Thuwis *et al.*[15] also present related FSI analyses for morphing aircraft applications.

III. Fish Bone Active Camber Concept

The Fish Bone Active Camber (FishBAC) mechanism provides an alternative design architecture to the concepts discussed above. Introduced by Woods and Friswell[16], this design employs a biologically inspired compliant structure to create large, continuous changes in airfoil camber and section aerodynamic properties. The structure consists of a thin chordwise bending beam spine with stringers branching off to connect it to a pre-tensioned Elastomeric Matrix Composite (EMC) skin surface. Both core and skin are designed to exhibit near-zero Poisson's ratio in the spanwise direction. Pre-tensioning the skin significantly increases the out-of-plane stiffness and eliminates buckling when morphing. Smooth, continuous bending deflections are driven by a high stiffness, antagonistic tendon system. Actuators mounted in the D-spar drive a tendon spooling pulley through a non-backdrivable mechanism (such as a low lead angle worm and worm gear). Rotation of the pulley creates equal but opposite deflections of the tendons. These differential displacements generate a bending moment on the rigid trailing edge strip, which then induces bending of the trailing edge morphing structure to create large changes in airfoil camber. A schematic overview of the FishBAC concept is shown in Figure 1. Since the tendon system is non-backdrivable, no actuation energy is required to hold the deflected position of the structure, reducing control action and power requirements. Furthermore, the automatic locking action of the non-backdrivable mechanism allows the stiffness of the tendons to contribute significantly to the chordwise bending stiffness of the trailing edge under aerodynamic load, without increasing the amount of energy required to deflect the structure.

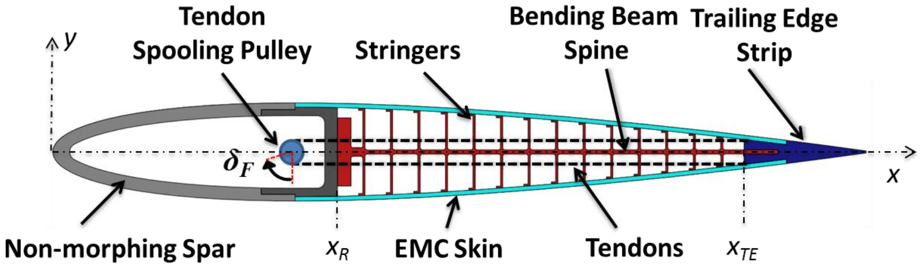

Figure 1. Fish Bone Active Camber concept

Wind tunnel testing of the prototype seen in Figure 2 found the FishBAC provided improved aerodynamic efficiency compared to traditional trailing edge flaps, with increases in lift-to-drag ratio of 25% being realized at equivalent lift conditions.[17] An increase in lift coefficient of $\Delta C_l = 0.72$ between unmorphed and morphed was measured at a freestream velocity of $V_\infty = 20$ m/s and an angle of attack of $\alpha = 0°$.

The large achievable deflections and continuous compliant architecture make this concept universally applicable to fixed wing applications ranging in scale from small UAVs to commercial airliners, and to rotary wing applications including wind turbines, helicopters, tilt-rotors, and tidal stream turbines.

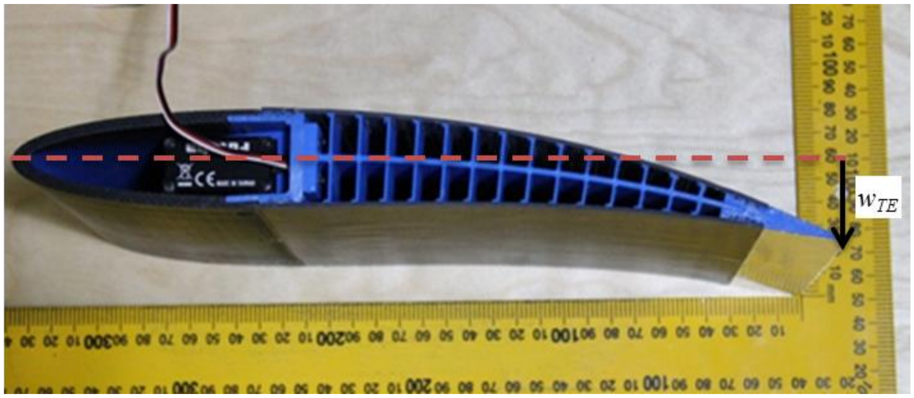

Figure 2. FishBAC wind tunnel test model showing deflected shape

IV. Fluid-Structure Interaction Analysis

The FSI analysis developed for the FishBAC structure uses two partitioned codes to separately analyze the aerodynamics and structural mechanics, with the antagonistic tendon actuation system being incorporated into the structural mechanics. These codes are coupled and iterated until convergence is achieved for all the relevant aerodynamic coefficients, as shown schematically in Figure 3. The mismatch in stiffness between the stiff tendon drive system and the aerodynamic load requires the use of a relaxation parameter to ensure stability of convergence.

Two different relaxation parameter algorithms were investigated in this work, and evaluated based on the speed and stability of their convergence.

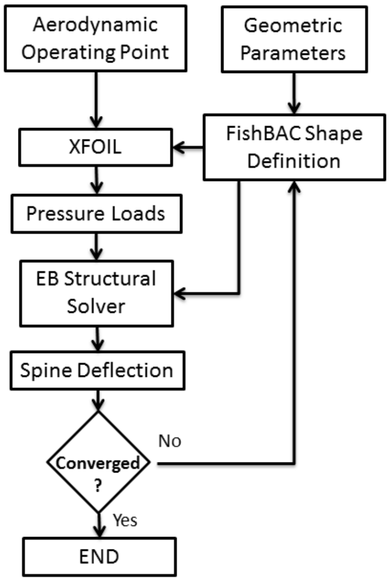

Figure 3. FSI algorithm schematic

A. Airfoil Definition and Deflection Parameterization

In order to ensure compatibility between the aerodynamic and structural solvers, the parameterization of the airfoil shape must be consistent for both. This was accomplished by independently defining the thickness distribution and the neutral axis deflection. In this way, the definition of the skin surface geometry required for the aerodynamic solver could be found for any deflected shape by superimposing the known thickness distribution onto the neutral axis position. A symmetric, uncambered NACA 0012 airfoil was used as the baseline for the FishBAC design shown here, and the internal bending core, tendons, and eleastomeric skin were also symmetric in their geometry and properties. Due to this, the neutral axis lies at the center of the airfoil, following the chord line of the undeformed state. The presence of the stringers in the FishBAC design serves to enforce the original thickness distribution in the skin, even with large trailing edge deflections. While the skin does experience small out-of-plane deflections between the stringers, they are of small magnitude and their effect on the overall bending stiffness of the FishBAC is ignorable, especially given the low stiffness of the skin. The effect of these local skin deflections on aerodynamic performance is perhaps not negligible, as will be discussed in further detail in the Aerodynamic Model section. Due to the structural symmetry and stringer enforced thickness distribution, the FishBAC airfoil can be parameterized as a constant thickness distribution overlaid onto the deflected shape of the bending beam spine. It is important, however, to account for curvature effects by adding the thickness distribution in a direction which is locally normal to the bending spine, especially given the large amount of camber obtainable with this concept. This approach is equivalent to the methodology used to define cambered airfoils for the NACA 4-digit series airfoils.[18]

Only the portion of the airfoil behind the rigid D-spar is considered in the structural model of the FishBAC, but the entire outer skin surface is needed for the aerodynamic analysis. The rigid D-spar ends and the morphing section begins at the non-dimensional chord location, x_R, and the morphing section continues until the beginning of the rigid trailing edge strip, x_{TE}, as labeled in Figure 1. It is important to note that while the rigid leading edge is not included in the structural model of the FishBAC, the trailing edge is. This is because even though it is assumed rigid and does not undergo any strains of its own, it does carry aerodynamic pressure loads which must be resolved as shear forces and bending moments through the spine.

The deflected shape of the bending spine is parameterized over the range of non-dimensional chord values [$x_R < x < x_{TE}$] by fitting a sixth-order polynomial to the predicted shape at a given iteration. Using a high order polynomial allows for complex deformation shapes to be readily captured, ensuring that the impact of any reflex or other inflections (either desired or undesired) in the spine shape can be properly accounted for in the aerodynamic analysis. It should be noted however, that the deflection of the bending beam spine is not restricted to a sixth-order polynomial during structural analysis. As will be discussed below, the spine is free to assume whatever continuous deflected shape the loading and stiffness distributions dictate. The polynomial coefficients are fitted to the shape of the bending beam after it is determined for a given iteration.

B. Aerodynamic Model

The aerodynamic pressure distribution acting on the FishBAC is found using the XFOIL panel method code. This code includes a viscous boundary layer component to predict skin friction drag and flow separation, offering a more complete drag prediction than inviscid codes. The code requires as inputs the aerodynamic conditions, [Mach number, $M_{\#}$, angle of attack, α, and Reynolds number, Re] and the non-dimensionalized airfoil skin coordinates. Using a viscous formulation of linear vorticity potential flow theory, XFOIL then calculates the distribution of pressure coefficient over the airfoil. Figure 4 shows a typical result of the pressure coefficient distribution over the upper and lower surfaces of the entire airfoil. The lift, drag and moment coefficients for the current airfoil shape are found by XFOIL from this pressure coefficient distribution.

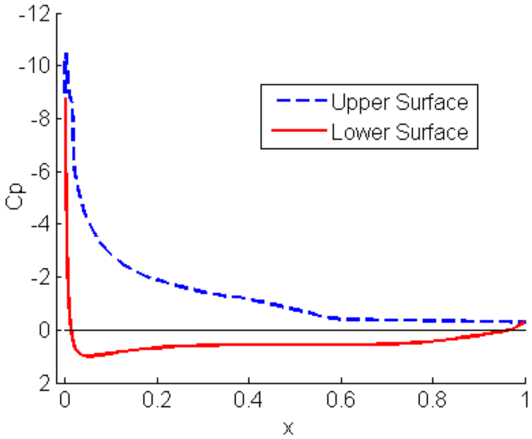

Figure 4. Representative distribution of pressure coefficient

For the structural component of this FSI problem, we consider distribution of the dimensional pressure acting only on the morphing portion of the chord ($x_R < x < x_{TE}$). Furthermore, since deformations in the thickness direction are not considered in this analysis (since the thickness distribution is maintained by the stringers), the pressure on the lower and upper skins can be combined to create a net pressure which acts on the spine as a chordwise varying distributed load, p, as shown in Figure 5. For this analysis, the net pressure distribution is applied directly to the bending spine. While in reality the load application would be more discretized, with each stringer carrying a locally integrated skin pressure load into its discrete attachment point with the spine, the number of stringers is fairly large and the changes in pressure are gradual enough that applying a continuous pressure load is a reasonable simplifying assumption.

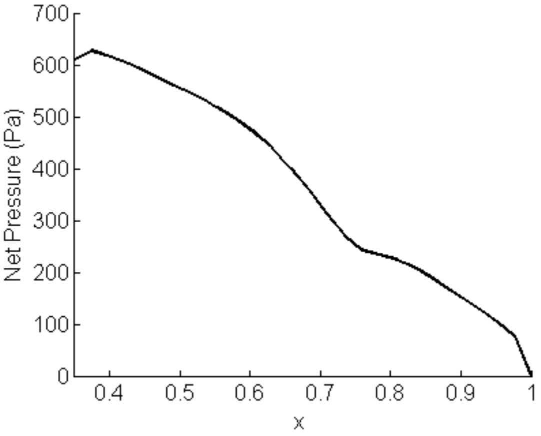

Figure 5. Representative net pressure distribution

The local out-of-plane deformations of the skin in between stringers in not directly considered in this FSI analysis. This is driven by the fact that the aerodynamic code used does not have high enough fidelity to accurately resolve the changes in aerodynamic pressure created by such deflections. While this is a limitation that could only be completely overcome by a higher fidelity (and therefore more computationally expensive) aerodynamic component, the impact of this assumption is mitigated by two factors. Firstly, the pre-tensioning employed in the elastomeric skin of the FishBAC concept significantly reduces the magnitude of any out-of-plane deflection, and secondly, the aerodynamic pressure acting on the morphing region of the FishBAC is much smaller than that seen on the rigid leading edge spar, as can be seen in Figure 4.

C. Structural Model

The derivation of the analytical formulation for morphing section stiffness from Euler-Bernoulli beam theory will be shown, the boundary conditions will be presented, and the distribution of flexural rigidity along the chord will be formulated. The antagonistic tendon actuation system is included in the structural model (although the driving actuator itself is not), so the kinematics and stiffness formulations of the tendons are also specified. The bending moments produced by the tendons are included into the integration of the Euler-Bernoulli equations.

1. *Governing Equations*

The structural model used in this FSI analysis is analytical and derived from Euler-Bernoulli beam theory. The low bending stiffness and high length to thickness ratio of the bending spine, low in-plane stiffness of the skin, and the continuous loading along the span make Euler-Bernoulli theory a good initial approximation for analysis. Furthermore, the high stiffness stringers branching off from the spine help to enforce the 'plane sections remain plane' assumption which underlies the derivation of Euler-Bernoulli beam theory.[19] Furthermore, empirical evidence, such as Figure 2, indicates that bending deformations do indeed dominate over shear deformations, as seen by the normal orientation of the stringers relative to the spine.

The bending deflections of the morphing structure are found by integrating the aerodynamic pressure distribution to find shear distribution, integrating that to find moment distribution, integrating again to find the distribution of slope, and then integrating one final time to find the deflection of the neutral axis. The effect of the actuation moments from the tendon system are added as additional bending moment during this integration process.

The relationship between net aerodynamic pressure, *p*, flexural rigidity, *EI*, and vertical displacement, *w*, is given by the Euler-Bernoulli beam equation:[19]

$$\frac{d^2}{dx^2}\left(EI(x)\frac{d^2w}{dx^2}\right) = p(x) \tag{1}$$

Integrating pressure produces force, specifically the vertical shear force acting on the beam:

$$\frac{d}{dx}\left(EI(x)\frac{d^2w}{dx^2}\right) = \int_{x_r}^{1} p(x)dx = V(x) \tag{2}$$

The integral of shear force is bending moment:

$$EI(x)\frac{d^2w}{dx^2} = \int_{x_r}^{1} V(x)dx = M(x) \tag{3}$$

The curvature of the spine can be found by rearranging Equation 3:

$$\frac{d^2w}{dx^2} = \frac{M(x)}{EI(x)} \tag{4}$$

Curvature is then integrated to give slope:

$$\frac{dw}{dx} = \int \frac{M(x)}{EI(x)}dx = \theta(x) \tag{5}$$

And finally, integrating slope provides the distribution of vertical deflection:

$$w = \int \theta(x)dx \tag{6}$$

2. *Boundary Conditions*

The integration constants which are generated during the solution of the Euler-Bernoulli equations are solved for by considering the boundary conditions. For the FishBAC, the bending spine is assumed to be clamped at its attachment to the rigid D-spar, and the end of the trailing edge is assumed to be free. This leads to the following conditions:

$$w(x_r) = 0 \tag{7}$$

$$\theta(x_r) = 0 \tag{8}$$

$$M(1) = 0 \tag{9}$$

$$V(1) = 0 \tag{10}$$

3. *Flexural Rigidity Formulation*

The flexural rigidity (*EI*) distribution of the FishBAC structure is formulated as a linear superposition of its components in this analysis. The spine is modeled as a constant thickness beam, and since its neutral axis is coincident with that of the FishBAC structure as a whole, the flexural rigidity of the bending spine, EI_{bs}, is equal to:

$$EI_{bs} = \frac{E_{bs}}{12} b {t_{bs}}^3 \tag{11}$$

where E_{bs}, is the elastic modulus of the bending spine material, b is the span of the FishBAC segment and, t_{bs}, is the thickness of the bending spine. Note that the rigidity of the spine could be made to vary along the chord without changing the formulation or implementation of this analysis. Indeed, tapering the thickness or modifying the material properties of the spine is an effective means of controlling the deflected shape, and therefore aerodynamic properties, of the FishBAC. While the results presented here are for a constant thickness spine, current work by the authors seeks to exploit these design variables to optimize the structure for various performance metrics.

The skin has a low inherent flexural rigidity, but because it is attached at a considerable distance from the neutral axis of the FishBAC, its contribution to overall stiffness must be considered. The flexural rigidity of the skin on the FishBAC, EI_{sk}, is therefore modeled using the parallel axis theorem.[20] The upper and lower skins are considered separately and then added:

$$EI_{sk} = E_{sk}\left[\frac{1}{12} b {t_{sk}}^3 + b t_{sk} {r_l}^2\right] + E_{sk}\left[\frac{1}{12} b {t_{sk}}^3 + b t_{sk} {r_u}^2\right] \tag{12}$$

here E_{sk}, is the elastic modulus of the skin material and, t_{bs}, is the thickness of the skin, r_l, is the distance between the lower skin surface and the neutral axis and, r_u, is the equivalent distance for the upper skin surface. As with the spine, the skin in this initial analysis is a constant thickness along the chord. However, in this case the flexural rigidity in not constant with chord due to the changing thickness of the airfoil. Significant reductions in stiffness, and therefore actuation requirements, could likely be obtained with no detrimental effect on maximum out-of-plane displacement if the skin thickness were tapered to match the distribution of aerodynamic pressure coefficient. Due to their thinness in the chordwise direction, the stringers are assumed to have a minimal impact on global bending stiffness, and are therefore are not included in the structural rigidity of the FishBAC for this initial analysis. The total FishBAC flexural rigidity, EI_{tot}, is the linear sum of the spine and skin rigidities:

$$EI_{tot} = EI_{bs} + EI_{sk} \tag{13}$$

4. *Antagonistic Tendon Kinematics and Stiffness*

The effect of the tendon moment on the structure is incorporated by adding an additional moment to the calculated bending moment from aerodynamic loading. The tendon bending moment is applied at the anchor point for the fixed ends of the tendons, which coincides with the beginning of the rigid trailing edge, x_{TE}. The tendon moment results from strains induced by the prescribed spooling pulley rotation angle, δ_F, and the FishBAC bending induced strains. The tendon is mounted with a sizeable offset from the spine neutral axis to allow it to effectively induce bending moments, which then leads to significant changes in length in the tendon with deflection. Changes in tendon length change the force levels in the tendon and the applied bending moments on the trailing edge which result. The moment from the tendon and the FishBAC deformation are therefore highly coupled. To include the tendons in the FSI model, we must first calculate the kinematics of tendon length with actuation inputs and deflection, and then formulate the stiffness of the tendons to relate deflections to resulting applied moments.

The total change in tendon length is a combination of the change in length due to pulley rotation, Δl_0, and that due to deflection in the spine, Δl_w:

$$\Delta l_{tot} = \Delta l_0 + \Delta l_w \tag{14}$$

The initial change in length due to pulley rotation is found from the arc length formula from the spooling pulley radius, r_p, and the spooling pulley rotation angle, δ_F:

$$\Delta l_0 = r_p \delta_F \tag{15}$$

Additionally, deformations of the spine induce changes in length of the tendons since they are supported at a distance from the neutral axis. In the current design, the distance from the neutral axis is fixed and equal to the tendon offset at the trailing edge mounting point, y_{ten}. This is done by running the tendons through small orifices in the stringers at a constant distance from the neutral axis. While the tendon is free to move closer or further away from the neutral axis in the unsupported regions between stringers, it is assumed in this analysis that the stringer spacing is close enough that these deviations will be quite small in magnitude, and the changes in overall tendon deflection caused by them will be correspondingly small. Given this assumption, changes in tendon length due to spine bending can then be found by integrating the product of the bending spine curvature and the distance from tendon to neutral axis according to Euler-Bernoulli theory:[19]

$$\Delta l_w = \int_{x_R}^{x_{TE}} \frac{M(x)}{EI} y_{ten} \, dx \tag{16}$$

The stiffness of the tendon is found from linear elastic theory for an axial rod. The sliding motion between the tendons and the stringers is assumed to occur without friction, and the use of braided cord for the tendons gives them negligible inherent bending stiffness. The tendon stiffness, k_{ten}, is equal to:

$$k_{ten} = \frac{E_{ten} A_{ten}}{L_{ten}} \tag{17}$$

where the cross section area is found from the diameter:

$$A_{ten} = \frac{\pi}{4} {d_{ten}}^2 \tag{18}$$

The force in the tendon at a given deflection will then be:

$$F_{ten} = k_{ten} \Delta l_{tot} \tag{19}$$

And finally, the total bending moment applied to the trailing edge by both tendons can be found from:

$$M_{ten} = 2 F_{ten} y_{ten} \tag{20}$$

Note that both tendons contribute equally to the generation of moment, such that the total moment is twice that of a single tendon. While this may seem counterintuitive, this result can be explained as follows. Due to their equivalent distance from the neutral axis, both tendons in the antagonistic pair will experience the same magnitude of length change from pulley rotation and spine bending, however, the lower and upper tendons will have different directions of length change. Specifically, for the case of a downwards FishBAC morphing, the lower tendon will have a decreasing length due to initial pulley spooling and a decreasing length with increasing spine deflection. The upper tendon on the other hand, will have an increase in length due to initial pulley rotation and increasing length due to increased spine deflection. Countering the opposite signs of the upper and lower tendon deflections is the opposite sign of the bending moment created by each. A positive pulley rotation (clockwise) will produce an increasing tension force in the lower tendon, increasing the positive (flap down) moment it induces on the FishBAC. Similarly, a positive pulley rotation reduces the tension force on the upper tendon, decreasing the negative (flap up) moment it induces on the FishBAC. In this way, the stiffnesses of both tendons contribute to the moment applied to the trailing edge. The tendons can only carry tension however (due to their lack of compressive stiffness), and so if the elastic deflections in the upper tendon and the bending deflections in the spine are such that the total tendon extension is less than zero, it will no longer contribute to the system stiffness. Pre-tensioning the tendons sufficiently ensures this never happens. The pre-tension forces are balanced and so produce no net moment on the spine. Additionally, so long as the tendons do not leave their linear elastic range, pre-tensioning has no effect on tendon stiffness.

D. Relaxation Parameters

Fluid–Structure Interaction algorithms frequently include relaxation parameters to reduce the occurrence of large, divergent oscillations in the predicted displacements between iterations.[21] Relaxation parameters work by adding "damping" to the solution, whereby the solution is only partially moved towards the solution predicted for the next iteration. In this way, the change in forcing experienced is reduced, and the tendency to experience fluctuating solutions of increasing divergence is tempered. If properly formulated, relaxation parameters do not change the value of the final converged solution, although they do decrease the speed of convergence. Therefore, they can be thought of as trading computation speed for solution stability. They are particularly important in systems with large differences in the stiffness of the various components. In the case of the FishBAC, the tendons are significantly stiffer than the spine, which is stiffer than the aerodynamics; making relaxation essential for stability. Two different relaxation parameter formulations were considered in this work, namely fixed and Aitken relaxation parameters. While relaxation parameters are typically applied to the displacement boundary between structure and fluid,[21] it will be shown that convergence in this problem was considerably improved by also including a relaxation parameter on the predictions of tendon moment.

1. *Fixed Relaxation Parameter*

Additional "damping" can be added to the solution process by using a fixed relaxation approach which allows for adjustable weighting of the solution towards the previous result;

$$u_{i+1} = w_F \tilde{u}_{i+1} + (1 - w_F) u_i \tag{21}$$

where the fixed relaxation parameter, w_F, is a constant value tuned for the given analysis, and $\tilde{u}_{i+1}$ is the estimated solution for the next iteration. A value of w_F close to zero will lead to very slow but stable convergence, whereas values close to one will essentially remove the relaxation effect, with instability likely to result.

2. *Aitken Relaxation Parameter*

More sophisticated algorithms can often improve the speed of convergence without affecting stability by using adaptive relaxation parameters. A commonly used adaptive method is the Aitken relaxation parameter.[22] This method is computationally very cheap as it is calculated from the results of the two previous runs of the code, and therefore does not require additional FSI runs.[22] In this algorithm, the amount of difference between estimates, known as the residual, is used to predict the value of the Aitken relaxation parameter, w_A, which will produce a residual of zero. The relaxation is therefore adaptive to the conditions of the solution, which typically results in faster convergence. The general form of the solution using Aitken relaxation is:

$$u_{i+2} = u_{i+1} + w_{A,i+1}(\tilde{u}_{i+2} - u_{i+1}) \tag{22}$$

note that the Aitken relaxation parameter, w_A, is itself recursive, and is defined from:

$$w_{A,i+1} = w_{A,i} \frac{u_i - \tilde{u}_{i+1}}{u_i - \tilde{u}_{i+1} - u_{i+1} + \tilde{u}_{i+2}} \tag{23}$$

again, the parameters with tildes are estimated values, i.e. the raw output from the FSI before relaxation is applied.

3. *Application to FishBAC FSI*

Typically, relaxation parameters in FSI problems are applied to the solution of the displacement of the boundary between the fluid and the structure. Since the analysis here essentially has three coupled components (fluid, structure, and actuation tendons), applying a relaxation parameter to both the fluid–structure interface and the tendon–structure interface was found to significantly improve convergence. Specifically, the bending spine deflection, *w*, and the tendon moment, M_{ten} were relaxed. The need for this can be seen in Figure 6, which shows a representative convergence plot for lift coefficient. Three lines are plotted which show the impact of applying a fixed relaxation parameter to various parts of the solution. Note that if the relaxation is applied only to the spine, which represents the fluid–structure interface deflection, which is the typical approach of other FSI algorithms, then the solution quickly diverges. This is due to very large fluctuations in the tendon moment. Even small spine deflections cause significant changes in tendon length, which due to the high stiffness of the tendons generates very large magnitude bending moments, which quickly drives the solution to diverge.

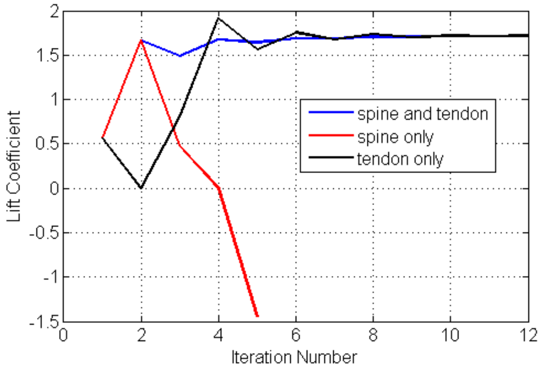

Figure 6. Application of fixed relaxation parameter to various system components

It can be seen in Figure 6 however, that applying a relaxation parameter to just the tendon solution is sufficient to stabilize the convergence of lift coefficient. Relaxing both the spine and the tendon produces the best result though, with a quick and stable approach with minimal overshoot being realized.

Comparing the Aitken relaxation to the fixed relaxation gives another interesting result. As can be seen in Figure 7, the fixed relaxation parameter is found to provide faster convergence. While the particular values used for the fixed relaxation have been tuned (whereas the Aitken parameter is essentially self-tuning) the values chosen work well over a range of angles of attack, free stream velocities and actuator settings. The results shown below will therefore use fixed relaxation parameters on both the spine and tendons.

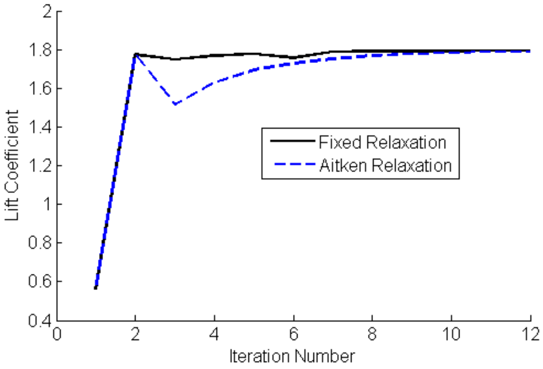

Figure 7. Comparison of lift coefficient convergence for fixed and Aitken relaxation parameters

V. Results and Discussion

This section will present results generated by the FishBAC FSI analysis for a representative geometry and aerodynamic operating point. Initially, the results of each step in the structural and aerodynamic solvers will be shown for a baseline case, followed by the convergence histories of the aerodynamic parameters of interest. Results for different tendon spooling pulley rotation angles, δ_F, will be plotted, to show the effect of actuation and the resulting morphing. Finally, the impact of actuation will be shown directly, by plotting the increases in lift, drag, and tendon moment that occur with tendon spooling pulley rotation.

The test case used for these results was chosen to match the operating conditions of the Swansea University wind tunnel, such that the FSI code could be used to design experimental test models. The relevant geometric and aerodynamic parameters are listed in Table 1.

Table 1. FishBAC parameters used for FSI test case

Parameter	Value	Units
baseline airfoil	NACA 0012	–
chord, c	0.3	m
span, b	0.15	m
end of rigid spar, x_R	0.35	–
trailing edge start, x_{TE}	0.85	–
skin thickness, t_{sk}	1.5	mm
skin modulus, E_{sk}	3.18	MPa
spine thickness, t_{bs}	2.0	mm
spine modulus, E_{bs}	2.14	GPa
tendon offset, y_{ten}	4.4	mm
tendon diameter, d_{ten}	1	mm
tendon modulus, E_{ten}	131	GPa
freestream vel., V_∞	20	m/s
angle of attack, α	5	deg
tendon pulley angle, δ_F	0–50	deg

The aerodynamic loading produced by the range of tendon pulley rotation angles studied is shown in Figure 8. It can be seen that increasing pulley rotation leads to an increase in the pressure loading. The net pressure results in Figure 8b show an interesting trend of a dip in pressure that's moves inwards from the trailing edge with increasing pulley rotation. This is likely the point of flow separation, which would be expected to move towards the leading edge as the bending deflections grow and the adverse pressure gradient on the upper surface becomes steeper.

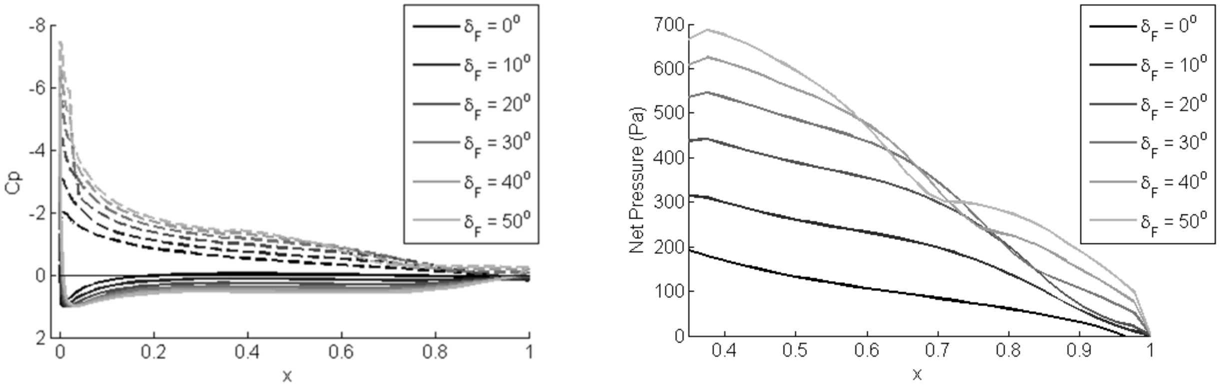

(a) (b)

Figure 8. Aerodynamic loading for test case a) pressure coefficient [dashed lines = upper surface, solid lines = lower surface] and b) net pressure over morphing region

The FSI code integrates the net pressure results from Figure 8b to produce the vertical shear force distributions seen in Figure 9a. Note that the magnitude of the forces increase with pulley rotation, although there is less change with higher rotation angles due to the progression of flow separation seen in Figure 8. Figure 9b shows the bending moment produced by integration of the shear forces. Note that these results also include the tendon moment. The tendon moment has the effect of shifting the bending moment down by a constant amount over the range $x_R < x < x_{TE}$, with the amount of shift increasing with pulley rotation angle. This is the expected result since larger pulley rotations would be expected to generate larger actuation moments, and as will be seen, larger displacements. Integrating bending moment and accounting for the flexural rigidity distribution gives the slope results shown in

Figure 9c. It is interesting to note that for $x > x_{TE}$, the slope is constant. This is the result of the rigid trailing edge strip not deforming. The final integration step produces the bending spine displacements shown in Figure 9d. As expected, the displacement increases with pulley rotation angle. Also, despite the sharp discontinuity in the bending moment distribution caused by the location of the tendon moment application, the final deflected shape of the spine is continuous. The maximum displacement of w_{TE} = 55.4 mm occurs when δ_F = 50°, and is equal to 18% of the chord.

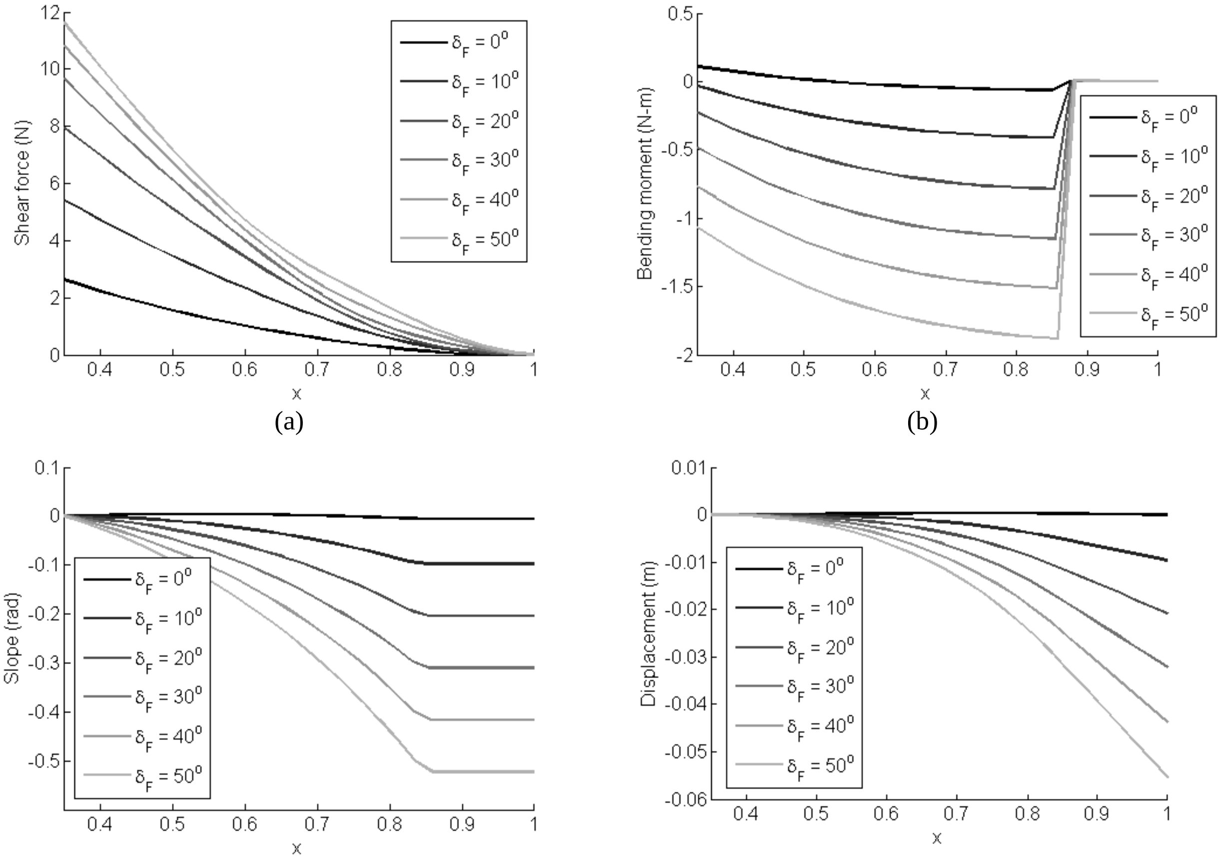

(a) (b)

(c) (d)

Figure 9. Structural results for the test case a) shear force, b) bending moment, c) slope, and d) bending spine displacement

By overlaying the airfoil thickness distribution on the bending spine displacements, we can see the predicted shape of the morphed FishBAC airfoil. Figure 10 shows these profiles for the range of tendon pulley rotation angles studied, along with a schematic representation of the spooling pulley rotation drawn to scale. Figure 10 highlights one of the limitations inherent to the Euler–Bernoulli formulation used here, which is the neglecting of any chordwise motion of the end of the trailing edge. Due to the fixed length of the bending spine, the trailing edge would in reality experience a small amount of chordwise motion, moving to the left as it bends down. While the overall deflections shown here are quite large (as desired for high control authority) the bending strains in the spine itself, which is only 2 mm thick, are quite small. The skin experiences larger strains, but is made of elastomer which is capable of very high strain levels and is of relatively low stiffness. This implies that the components of the FishBAC structure are likely to still be operating in their linear ranges despite the large overall strain levels. The validity of this assumption is of course subject to experimental validation, but work is ongoing to this end.

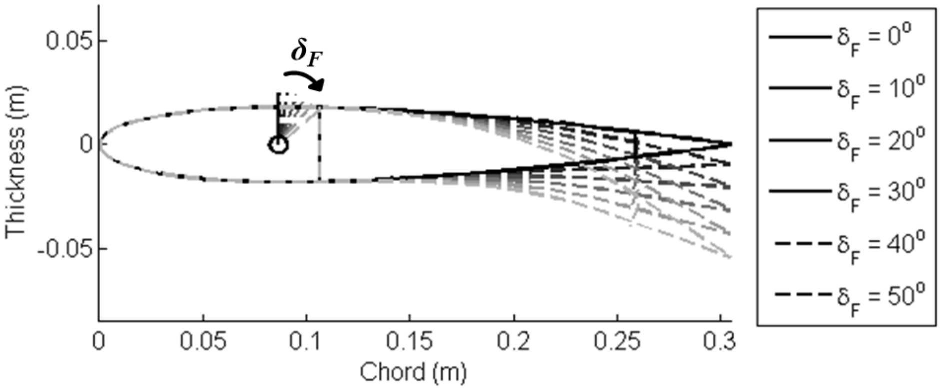

Figure 10. Equilibrium deflected FishBAC shapes

It is useful to consider the impact of tendon pulley spooling angle on the convergence of the aerodynamic coefficients. Of primary interest here are the lift and drag coefficients visible in Figure 11. Here several interesting behaviors can be noted. Firstly, in Figure 11a it can be seen that increasing pulley rotation increases lift coefficient. This is an expected result stemming from the increased spine deflections seen in Figure 9d, which would increase airfoil camber and thus lift. There is a diminishing return however on the amount of additional lift developed with each ten degrees increment of pulley rotation. This is likely to be a direct result of the pressure loss resulting from the flow separation discussed above. Despite this, the predicted range of achievable lift coefficients is quite large, with a $\Delta C_l = 1.21$ at the chosen operating point. Also note that the convergence behavior is very stable across the entire δ_F range, with convergence occurring in 4–5 iterations. The drag results present an interesting counterpoint. The drag coefficient in Figure 11b is seen to grow at an accelerating rate with increasing pulley rotation. This is due to the large drag induced by the onset of flow separation. Furthermore, while the convergence is again stable across the entire range, the number of iterations required to get a converged result increases with pulley rotation where before it was essentially independent of δ_F. This indicates drag is more sensitive to spine shape than lift.

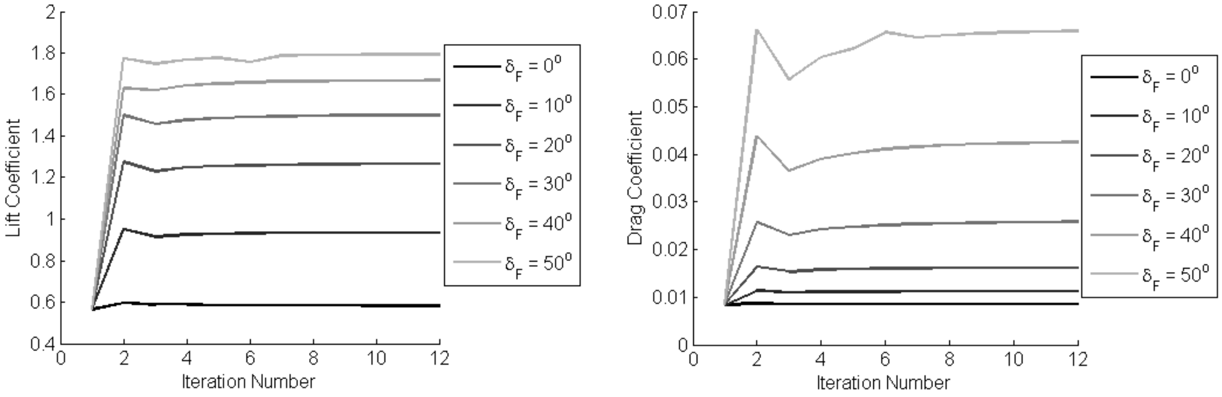

(a) (b)

Figure 11. Convergence of aerodynamic coefficients a) lift and b) drag

The effect of pulley rotation on lift and drag can be considered more directly by looking at only the final converged results, and by running the FSI code for a finer sweep of rotation angles. Figure 12 shows the results for lift and drag with δ_F swept from 0° to 50° in 2.5° increments. The trends mentioned above can now be seen in more detail. Figure 12a shows the diminishing returns in lift achieved with pulley rotation. The results do not seem to have plateaued however, indicating that still higher lift coefficients are theoretically possible. The realistic impact of this is fact is probably moot however, as XFOIL is generally not-conservative in its lift and drag estimates, and real flow conditions in a wind tunnel or in free flight would likely lead to more rapid and extensive flow separation and therefore lower lift coefficients. Indeed, $C_l = 1.8$ is a very high figure to achieve with a single element airfoil with no boundary layer control.[23] Similarly, the drag coefficients predicted in Figure 12b are likely to be lower than those experienced experimentally. These limitations in XFOIL are well known, and not a problem from a design standpoint so long as they are properly accounted for. Given the analytical nature of the results presented here, experimental validation is ultimately required, and work to this end is ongoing.

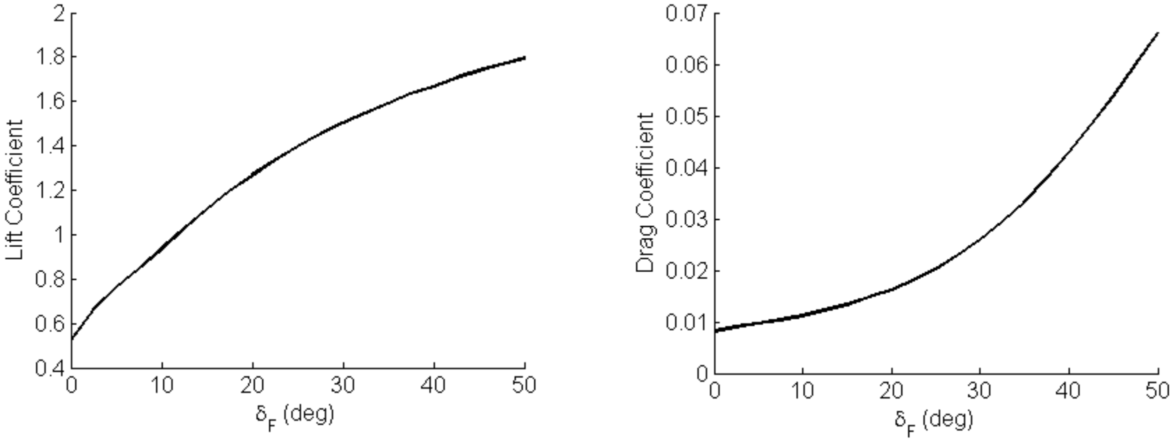

(a.) (b.)

Figure 12. Evolution of aerodynamic coefficients with actuation, a) lift and b) drag

Another useful aspect of this FSI code is its ability to predict actuation requirements. By prescribing the tendon spooling pulley rotation angle (equivalent to the required actuator output rotation) and then solving for the resulting moments generated by the tendons, the reaction moment that the actuator is required to maintain is automatically known. Figure 13a shows the relationship between pulley rotation and required moment, and Figure 13b shows the evolution of predicted lift coefficient with actuation moment. From a design standpoint, this is a very useful feature of the code, since it allows for the actuation system to be sized appropriately

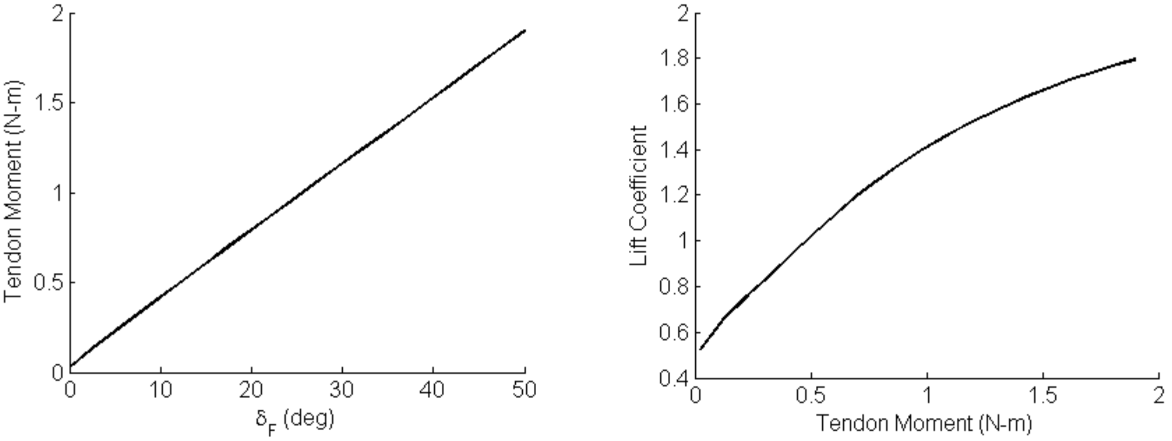

(a.) (b.)

Figure 13. Actuation moments, a.) moment versus spooling pulley rotation, and b.) lift versus moment

VI. Conclusion

This work has presented the development of a highly coupled, partitioned fluid–structure interaction analysis of the Fish Bone Active Camber mechanism. An analytical structural model based on Euler-Bernoulli beam theory is developed and shown to be applicable to the specific design case of the FishBAC structure. The XFOIL inviscid panel method code is used to solve for the aerodynamic pressure acting on the morphing structure at each iteration. The impact of the antagonistic tendon system used to drive the morphing deflections is included in the structural formulation. Due to large differences in stiffness between the aerodynamics, actuation, and structure, stable convergence of the solution is found to require the application of relaxation parameters at the fluid–structure interface and the tendon–structure interface. While both fixed and Aitken relaxation parameters are considered, a fixed relaxation parameter is used in the results presented here due to significantly faster convergence. The various results of the FSI analysis are then shown for a representative geometry and aerodynamic operating point. Using this analysis the FishBAC is shown to be capable of a large control authority in lift coefficient, with drag and actuation behaviors that are reasonable.

In conclusion, the FSI analysis presented here is found to be a capable and robust tool for understanding and predicting the behavior of the novel and promising Fish Bone Active Camber morphing airfoil concept.

VII. Acknowledgements

The research leading to these results has received funding from the European Research Council under the European Union's Seventh Framework Programme (FP/2007-2013) / ERC Grant Agreement n. [247045].

VIII. References

[1] Chopra, I., “Status of Application of Smart Structures Technology to Rotorcraft Systems,” *Journal of the American Helicopter Society*, 2000, Vol. 45, pp.228-252.

[2] Giurgiutiu, V., “Recent Advances in Smart-Material Rotor Control Actuation,” Proceedings of the AIAA/ASME/ASCE/AHS/ASC 41st Structures, Structural Dynamics and Materials Conference, Atlanta, GA, April 3-6, 2000, AIAA-2000-1709.

[3] Barbarino, S., Bilgen, O., Ajaj, R.M., Friswell, M.I., Inman, D.J., “A Review of Morphing Aircraft,” *Journal of Intelligent Material Systems and Structures*, June 2011, Vol. 22, No. 9 pp. 823-877.

[4] Straub, F., Kennedy, D. K., Stemple, A. D., Anand, V. R., and Birchette, T. S.,. “Development and Whirl Tower Test of the SMART Active Flap Rotor,” SPIE Smart Structures and Materials, San Diego, CA, March 14-18, 2004.

[5] Dieterich, O., Enenkl, B., and Roth, D. 2006. “Trailing Edge Flaps for Active Rotor Control: Aeroelastic Characteristics of the ADASYS Rotor System,” 62th Annual Forum of the American Helicopter Society, Phoenix, Arizona, May 9-11.

[6] Grohmann, B., Maucher, C., Prunhuber, T., Janker, P., Dieterich, O., Enenkl, B., Bauer, M., Ahci, E., Altmikus, A., Baier, H., “Multidisciplinary Design and Optimization of Active Trailing Edge for Smart Helicopter Rotor Blade,” *Mechanics of Advanced Materials and Structures*, 2008, Vol. 15, No. 3, 307-324.

[7] Bartley-Cho, J.D., Wang, D.P., Martin, C.A., Kudva, J.N., West MN. Development of high-rate, adaptive trailing edge control surface for the smart wing phase 2 wind tunnel model. *Journal of Intelligent Material Systems and Structures* 2004, 15: 279–291.

[8] Daynes, S., and Weaver, P.M., “Morphing Blade Fluid-Structure Interaction”, 53rd AIAA/ASME/ASCE/AHS/ASC Structures, Structural Dynamics, and Materials Conference, 2012, pp. 1-15.

[9] Bae, J.S., Kyong, N.H., Seigler, T.M., and Inman, D.J., “Aeroelastic considerations on shape control of an adaptive wing” *Journal of Intelligent Material Systems and Structures,* 2005, Vol. 16, pp. 1051–6.

[10] Campanile, L.F., and Anders, S., “Aerodynamic and aeroelastic amplification in adaptive belt-rib airfoils,” *Aerospace Science and Technology*, Vol. 9, pp. 55–63.

[11] Barbarino, S., Pecora, R., Lecce, L., Concilio, A., Ameduri, S., and Calvi, E., “A novel SMA-based Concept for Airfoil Structural Morphing,” *Journal of Materials Engineering and Performance*, 2009, Vol. 18, No. 5, pp. 696-705.

[12] Bilgen O, Saavedra Flores E.I. and Friswell M.I., “Optimization of surface-actuated piezo composite variable-camber morphing wings,” Proceedings of the ASME Conference on Smart Materials, Adaptive Structures and Intelligent Systems, Sept. 18-21, 2011, Scottsdale, AZ.

[13] De Gaspari, A., and Ricci, S., “A two-level approach for the optimal design of morphing wings based on compliant structures,” Journal of Intelligent Material Systems and Structures, Vol. 22, No. 10, pp. 1091–111.

[14] Molinari, G., Quack, M., Dmitriev, V., Morari, M., Jenny, P., and Ermanni, P., “Aero-structural optimization of morphing airfoils for adaptive wings,” *Journal of Intelligent Material Systems and Structures*, 2011, Vol. 22, pp. 1075–89.

[15] Thuwis, G.A., Abdalla, M.M., and Gurdal, Z.,“Optimization of a variable-stiffness skin for morphing high-lift devices,” *Smart Materials and Structures,* 2010, Vol. 19, 124010.

[16] Woods, B.K.S., and Friswell, M. I., “Preliminary Investigation of a Fishbone Active Camber Concept,” *Proceedings of the ASME 2012 Conf. on Smart Materials, Adaptive Structures and Intelligent Systems*, Sept 19-21, 2012, Stone Mountain, GA.

[17] Woods, B.K.S., Bilgen, O., and Friswell, M.,I., “Wind Tunnel Testing of the Fishbone Active Camber Morphing Concept,” Proceedings of the 23rd International Conference on Adaptive Structures and Technologies, October 11-13, 2012, Nanjing, China.

[18] Abbott, I., and Von Doenhoff, A., *Theory of Wing Sections*, Dover Publications, New York, 1958, pp. 190-197.

[19] Meirovitch, L., *Fundamentals of Vibration*, McGraw-Hill, New York, NW, 2001.

[20] Hall, A.S., Archer, F.E., and Gilbert, R.I., *Engineering Statics*, 2nd Edition, UNSW Press, Sydney, Australia, 1999.

[21] Hou, g., Wang, J., Layton, A., “Numerical Methods for Fluid-Structure Interaction – A Review,” *Communications in Computational Physics*, Vol. 12, No. 2, August 2012, pp. 337-377

[22] Irons, B., and Tuck, R.C., “A version of the Aitken accelerator for computer implementation,” *International Journal for Numerical Methods in Engineering*, 1969, Vol. 1, pp. 275–277.

[23] Raymer, D.P., *Aircraft Design: A Conceptual Approach*, 3rd Edition, AIAA Inc, Reston, VA, 1999.